frontiers in Materials

ORIGINAL RESEARCH
published: 11 December 2020
doi: 10.3389/fmats.2020.564624

Friction and Wear Behaviors of Reduced Graphene Oxide- and Carbon Nanotube-Reinforced Hydroxyapatite Bioceramics

Huanlong Hu[1], *Zhong Li*[1,2]*, *Wen Sun*[1], *Ruitao Li*[1,3], *Hua Li*[1] *and Khiam Aik Khor*[1]*

[1]School of Mechanical and Aerospace Engineering, Nanyang Technological University, Singapore, [2]Center for Cellular and Molecular Engineering, Department of Orthopaedic Surgery, University of Pittsburgh School of Medicine, Pittsburgh, PA, United States, [3]School of Mechanical Engineering, Jiangsu University, Zhenjiang, China

Friction and wear properties play an important role in the long-term *in vivo* performance of load-bearing bioceramic implants. In this study, the friction and wear behaviors of hydroxyapatite (HA) reinforced with reduced graphene oxide (rGO) and rGO + carbon nanotube (CNT) hybrids were studied by ball-on-disk tests to understand the effects of nanocarbon content and morphology on the composites' tribological behaviors. The intact and worn surfaces were characterized by optical microscopy, nanoindentation, field emission scanning electron microscopy, energy-dispersive X-ray spectroscopy, and Raman spectroscopy. We found that the incorporation of rGO and rGO + CNT hybrids in HA bioceramic both improved the friction and wear behaviors, and the highest wear resistance was achieved by employing 1 wt% rGO and 1 wt% CNT as reinforcements. The major reinforcing mechanism was the formation of carbonaceous films between the composite surfaces and counterbody, which served as solid lubrication films that resulted in a lower coefficient of friction, higher hardness, and increased hardness/modulus ratio. Importantly, CNT addition facilitated the uniform distribution of the reinforcements in the HA matrix and the pinning effects of CNT enhanced the connection between rGO and HA.

Keywords: hydroxyapatite, carbonaceous reinforcement, structural characterizations, tribological behaviors, mechanical properties

OPEN ACCESS

Edited by:
Valeria Cannillo, University of Modena and Reggio Emilia, Italy

Reviewed by:
Zhang Qiao Xin, Wuhan University of Technology, China
Ilaria Cacciotti, University Niccolò Cusano, Italy

***Correspondence:**
Zhong Li
zli013@ntu.edu.sg
Khiam Aik Khor
mkakhor@ntu.edu.sg

Specialty section:
This article was submitted to Ceramics and Glass, a section of the journal Frontiers in Materials

Received: *26 May 2020*
Accepted: *03 November 2020*
Published: *11 December 2020*

Citation:
Hu H, Li Z, Sun W, Li R, Li H and Khor KA (2020) Friction and Wear Behaviors of Reduced Graphene Oxide- and Carbon Nanotube-Reinforced Hydroxyapatite Bioceramics. Front. Mater. 7:564624. doi: 10.3389/fmats.2020.564624

INTRODUCTION

The aging of the world's population creates an increasing demand for bone repair and regeneration, with over four million operations annually (Amini et al., 2012; Turnbull et al., 2018). While the use of autografts remains the gold standard treatment, they have very limited availability and can cause donor site morbidity. Allografts and xenografts, albeit with higher availability, pose risks such as disease transmission and detrimental immune responses (Martin and Bettencourt, 2018). A broad array of synthetic biomaterials, including ceramics, metals, polymers, and composites, have been utilized for orthopedic tissue engineering (Aminzare et al., 2013; Wang and Yeung, 2017). Bioceramics are among the most widely used materials for hard tissue repair. Among the diverse forms of bioceramics, hydroxyapatite ($Ca_{10}(PO_4)_6(OH)_2$, HA) has attracted significant attention because it is the main mineral component in bones and teeth of vertebrates; the biocompatibility, bioactivity, and osteoconductivity of HA have led to its extensive applications

in bone tissue engineering (Prakasam et al., 2015). Despite the outstanding biological properties of HA, the insufficient mechanical properties and wear resistance make monolithic HA bioceramics still problematic for load-bearing applications (Baradaran et al., 2014; Liu et al., 2016).

Friction and wear behaviors are important properties that determine the long-term performances of bioceramic implants, especially when used for the substitution of hip and knee joints (Fellah et al., 2015). Due to the complex biomechanical and biochemical environment in the human body, the implanted bioceramics are subjected to constant friction and wear, which is a main reason for the generation of wear debris and implant loosening (Beake and Liskiewicz, 2013). In addition, excessive abrasion causes a reduction of the implant's mechanical properties, contributing to early-failure of the device (Liu et al., 2014; Li et al., 2018).

To extend the clinical applications of bioceramics, the wear resistance of monolithic bioceramics can be improved by adding secondary carbonaceous reinforcements, such as carbon fibers (Lu et al., 2012) and graphite (Teoh et al., 1998). As nanosized carbonaceous materials, one dimensional (1D) carbon nanotubes (CNTs), and two dimensional (2D) graphene and graphene derivatives such as reduced graphene oxide (rGO), have outstanding physical and mechanical properties and have already shown their potential as reinforcements to improve biomaterials' tribological behaviors in bioceramic matrixes of Al_2O_3, HA, and yttria tetragonal zirconia polycrystals (Balani et al., 2008; Lahiri et al., 2010; Gutiérrez-Mora et al., 2019). It has already been demonstrated that the introduction of such nanofillers could markedly improve the overall and microscopic mechanical, friction and wear properties of the composites (Li X. et al., 2020). Furthermore, recent studies on the hybridization or heterostructuring of 1D CNT and 2D graphene used as reinforcements demonstrated improved mechanical and tribological properties of aluminum, magnesium, phenolic, and Cu matrixes (Li Z. et al., 2015; Wang et al., 2018; Li et al., 2019; Turan et al., 2019; Zhao et al., 2019). Such improvement was attributed to the enhanced dispersion state of the nanocarbon reinforcements and the synergistic strengthening effect of 1D and 2D reinforcements induced by the formation of a planar interconnected nano-reinforcement structure (Gao et al., 2017). In addition, rGO and CNT have been proved in a number of studies to be biocompatible when incorporated into bioceramics (Bianco, 2013; Notley et al., 2013; Li et al., 2014; Thompson et al., 2015). However, the application of graphene/CNT hybrids to reinforce bioceramics has not been well studied, and the tribological properties of such composites has been rarely reported. It is therefore of importance to chanracterize the tribological and mechanical behaviors of nanocarbon hybrid-reinforced composteis and explore the possible mechanisms underlying the potential reinforcing effects.

In the present work, we report the preparation of rGO and rGO/CNT hybrids reinforced HA composites, and rationalize their structural, mechanical, and tribological properties. This research aims to expand the applications of advanced bioceramics in load-bearing orthopedic implants through the improvement of their tribological behaviors.

MATERIALS AND METHODS

Sample Preparation

The HA nanorod powders used in this study were produced by a wet chemical precipitation method based on the following reaction and the detailed synthesis procedure was reported in our previous study (Li et al., 2017).

$$10\,Ca(OH)_2 + 6\,H_3PO_4 \rightarrow Ca_{10}(PO_4)_6(OH)_2 + 18\,H_2O \quad (1)$$

Briefly, diluted *ortho*-phosphoric acid (Merck, Singapore) was added dropwise through a peristaltic pump to the calcium hydroxide (>96% purity in powder, Merck, Singapore) solution until the pH value dropped below 9, with the solution temperature maintaining at 36.8°C. The HA nanorod precipitates were purified by several rounds of washing with DI water, and the concentration was determined to be 53.5 mg ml^{-1} by weighing the dried cake from a known volume of solution. Two types of nano reinforcements, rGO nanoplates and CNTs (65928, Sigma-Aldrich, St. Louis, MO) were used in this study. The diameter and length of CNTs were 110–170 nm and 5–9 μm, respectively. Cetyltrimethylammonium bromide (CTAB; H5882, Sigma-Aldrich, St. Louis, MO) was used as the surfactant to homogeneously disperse rGO and CNT in water.

A schematic of the sample preparation process is shown in **Figure 1**. HA and nanocarbon powders were ball milled (2 h, 180 rpm, Al_2O_3 balls) in DI water with CTAB (1.0 wt% CTAB to nanocarbons) added as the surfactant, followed by oven drying at 90°C for 12 h and grinding by a mortar and pestle to obtain fine composite powders. **Table 1** lists the designation and composition of the prepared composites.

The mixed powders were densified using an SPS system (Dr. Sinter 1050, Sumitomo Coal Mining, Japan). According to our previous experiments, the optimal sintering conditions for HA nanorods are 1,050°C dwell temperature, 100°C/min heating and cooling rates, and 3 min dwell time (Li Z. et al., 2020). Briefly, 0.6 g mixed powder was wrapped in a graphite foil and loaded in a cylindrical graphite die with an inner diameter of 10 mm. Two pieces of graphite foils were put between the punches and powder to prevent the reaction between the powder and die set and facilitate current flows. An initial temperature of 600°C was reached in 1 min and maintained for 3 min, followed by a ramp to 650°C in 1 min and subsequently to 1,050°C in 4 min. A pressure of ~8 MPa was applied initially, and the piston was free to move unless the pressure was above 30 MPa throughout the heating up period. After the temperature reached 1,020°C, the pressure was slowly increased to 50 MPa to inhibit abnormal temperature rise and maintained at this pressure during the dwell time. In the cooling period, the pressure was released to ~10 MPa. The sintering was performed in a vacuum environment with a residual pressure of ~4–6 Pa, and sintering temperature was regulated by an infrared pyrometer focused on a small hole in the outer wall of the die.

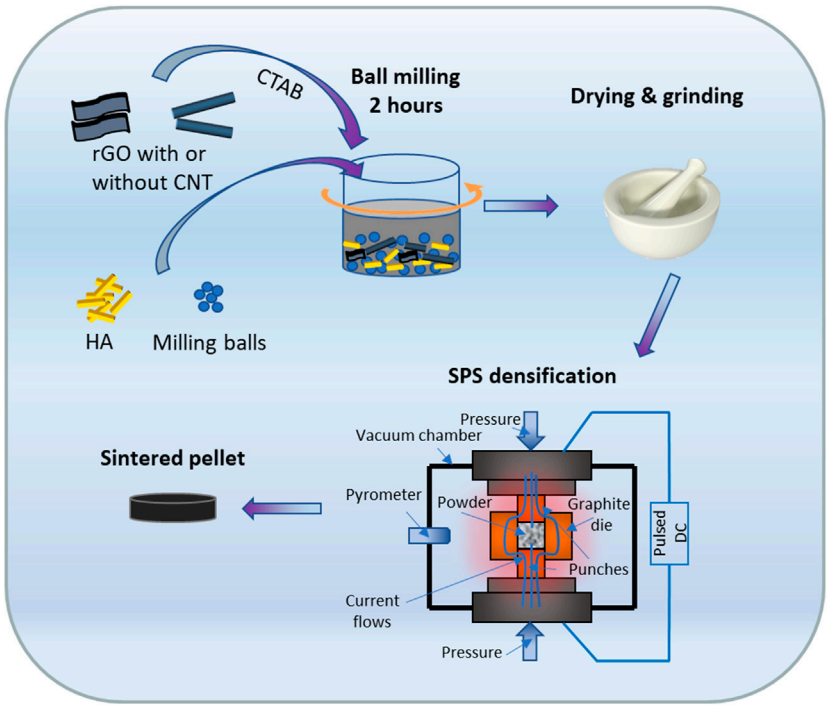

FIGURE 1 | Schematic illustrations of the powder mixing and densification processes.

TABLE 1 | Designation and composition of hydroxyapatite and nanocarbon-reinforced hydroxyapatite composites.

Designation	HA	1rGO	2rGO	0.5rGO+0.5CNT	1rGO+1CNT
HA (wt.%)	100	99	98	99	98
rGO (wt.%)	-	1	2	0.5	1
CNT (wt.%)	-	-	-	0.5	1

Wear Tests

The friction and wear performances of nanocarbon-reinforced HA composites were studied by a ball-on-disk micro-tribometer (Continuous Stiffness Measurement High-Temperature Tribometer, Switzerland). The counter surface was provided by a Si_3N_4 ball with a radius of 3 mm. A normal load (F_p) of 2 N was applied on the ball, which slid against the polished samples in a circular path (2 mm in diameter) for 10,000 laps at a sliding speed of 1.5 cm/s. Prior to the wear tests, the sintered pellets were sequentially ground using grit #400, #800, #1200, #2400, #4000 sandpapers, and polished with 1 and 0.25 µm diamond pastes to obtain mirror-like surfaces and cleaned with ethanol.

The wear volume (V) was calculated based on the width of wear tracks according to the following equation (Huang et al., 2017):

$$V = 2\pi R\left[r^2 sin^{-1}\left(\frac{w}{2r}\right) - \left(\frac{w}{4}\right)\sqrt{4r^2 - w^2}\right] \quad (2)$$

where R is the sliding radius, w the average width of the wear track and r the radius of the Si_3N_4 ball. w was measured by ImageJ software for at least three times and the standard deviation was reported. The wear rate of the plates (W) was calculated from the slope of wear volume vs. sliding distance and normal load (Ahmad et al., 2018):

$$W = \frac{V}{L \times F_p} \quad (3)$$

where V is the wear volume loss derived from **Eq. 2**, L is the sliding distance equal to 94.25 m, and F_p is the applied normal load.

Characterization

The morphology of the intact and worn surfaces of sintered samples was observed by optical microscopy (Zeiss Axioskop 2, United States) and field emission scanning electron microscopy (FESEM; JEOL JSM 7600F, Japan). The Energy-dispersive X-ray spectroscopy (EDS) analysis was conducted with the EDS detector (Oxford Instruments, United Kingdom) equipped with FESEM to compare the relative carbon content in different areas on the same

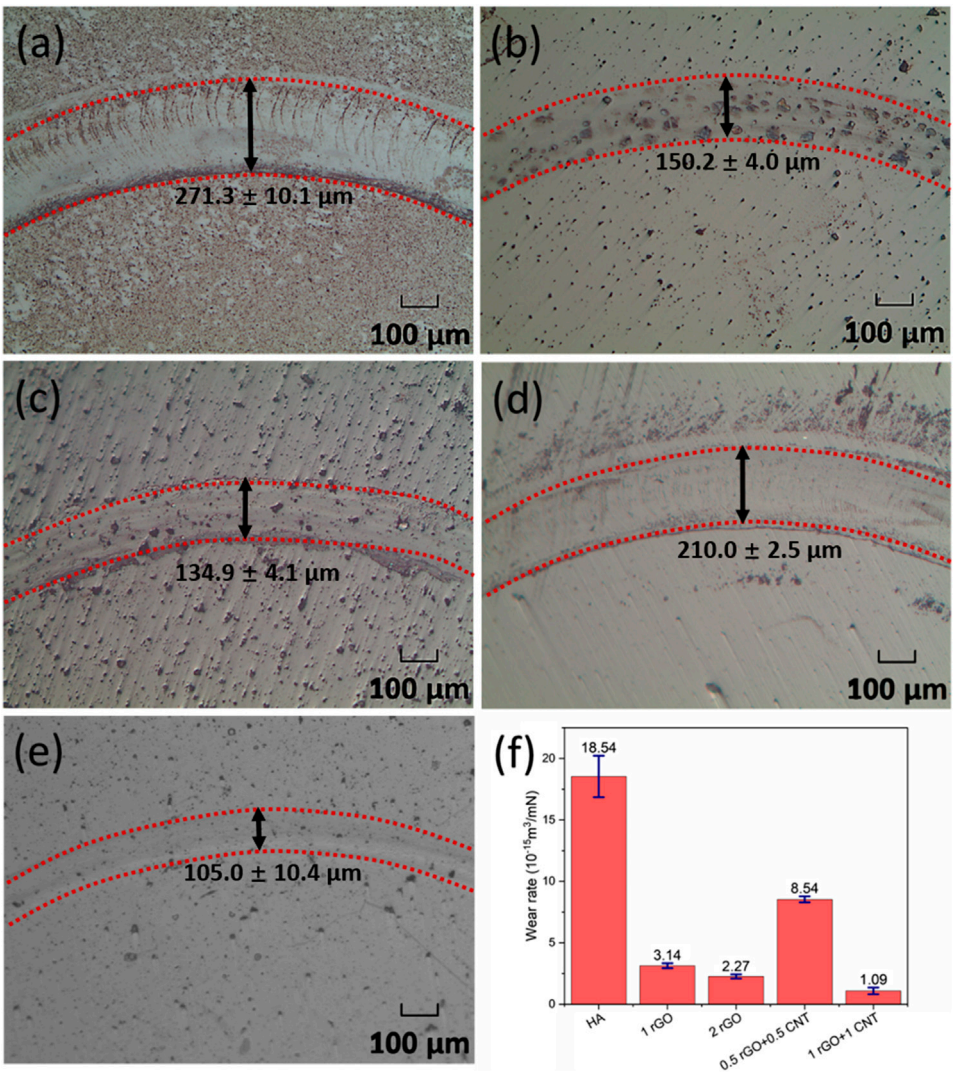

FIGURE 2 | Microscopic images of the wear tracks: **(a)** HA; **(b)** 1rGO; **(c)** 2rGO; **(d)** 0.5rGO+0.5CNT; **(e)** 1rGO+1CNT. The corresponding wear rates of the sintered bioceramics are given in **(f)**.

sample. Prior to FESEM observation, samples were cleaned with ethanol, mounted on the sample holder using conductive tape, and coated with platinum for 30 s. It is noted that the accelerating voltage used for FESEM imaging was 2 kV to avoid the charging effect, and was increased to 15 kV in EDS analysis to obtain sufficient signals.

Raman spectroscopy is a fast, nondestructive, and high-resolution tool for the characterization of the rGO and CNT based composites (Wu et al., 2018). Raman spectra of fresh and worn surfaces of rGO and CNT reinforced HA composites were collected using a Rapid Imaging MicroRaman spectrophotometer system (Renishaw Invia, United Kingdom) with a 488 nm line of a HeNe laser.

The Young's modulus and hardness of the sintered samples were measured using the Agilent Nano Indenter G200, which was operated under the continuous stiffness measurement mode. A Berkovich diamond tip (Micro Star Technologies B-style, tip radius ~20 nm) was used and the tip-area calibration was done using a standard fused silica substrate of known modulus (72 GPa). The depth limit, strain rate target, harmonic displacement target, and frequency target were set at 1,000 nm, 0.05 s^{-1}, 2 nm, and 45 Hz, respectively.

In nanoindentation tests, the total work (W_t) done by the penetration process can be divided into two parts:

$$W_t = W_e + W_p \tag{4}$$

where W_e and W_p correspond to the elastic and plastic work done, respectively. The ratio of W_p over W_t is used to indicate the materials' elastic-plastic properties (Cheng and Cheng, 2004; Lahiri et al., 2010):

$$\frac{W_p}{W_t} = 1 - \left[\frac{1 - 3\left(\frac{h_f}{h_m}\right)^2 + 2\left(\frac{h_f}{h_m}\right)^3}{1 - \left(\frac{h_f}{h_m}\right)^2}\right] \tag{5}$$

where h_m and h_f are the depth of the indent at peak load and the final one after elastic recovery, respectively.

RESULTS

Optical Microscopy and Wear Rate

Optical microscopy observations of the wear scars of various compositions (**Figures 2A–E**) show the width of wear scars, with the width values of wear scars marked in each Figure. In general, compared with pure HA, the wear track widths of the composites were reduced at higher total nanocarbon content, and the narrowest value was obtained in 1 wt% rGO and 1 wt% CNT-reinforced composites. Similar trend was reported by Yazdani et al. (2015) in the graphene nanoplates (GNPs)- and CNTs-reinforced Al_2O_3 system. The specific wear rates calculated from **Eqs. 2**, **3** are shown in **Figure 2F**. Pure HA pellet had a high wear rate of $18.55 \pm 2.07\times10^{-15}$ m^3/N·m and the addition of any kind of nanocarbon fillers to the HA matrix resulted in a significant improvement in wear resistance. In addition, this improvement was influenced by the loading content and morphology of the reinforcements. In terms of loading content, by increasing the total nanocarbon loading from 1 to 2 wt%, the wear resistances of both rGO- and rGO + CNT-reinforced composites were substantially increased. In rGO-reinforced HA composites, the wear rate was decreased from 3.14 ± 0.25 to $2.27 \pm 0.21\times10^{-15}$ m^3/N·m with an increase of filler loading from 1 to 2 wt%; in rGO + CNT composites, the decrease was more obvious, from $8.54 \pm 0.31\times10^{-15}$ m^3/N·m for samples with 1 wt% nanofiler to $1.09 \pm 0.32\times10^{-15}$ m^3/N·m for those with 2 wt% nanofiller. In terms of nanocarbon morphology, by comparing the rGO- and rGO + CNT- added composites with the same nanocarbon content, the wear rates differed a lot. At 1 wt% total nanocarbon loadings, 1 rGO had a lower wear rate than 0.5 rGO + 0.5 CNT, whereas at 2 wt% total nanocarbon loadings, 1 rGO + 1 CNT composites showed higher wear resistance than 2 rGO composites. Furthermore, compared with 1rGO added composites, the addition of 1 wt% rGO and 1 wt% CNT as reinforcements had further improved the wear resistance. Compared with pure HA sample, the lower standard deviations for nanocarbon-reinforced composites were possibly due to the improved electrical and thermal conductivities of the composites induced by the addition of nanocarbon reinforcements that facilitated more uniform structure of the composites in the spark plasma sintering process.

Coefficient of Friction

To assess the friction performance of the composites, the evolution of the coefficient of friction coefficient (COF) during the ball-on-disk tests of pure HA and nanocarbon reinforced composites were recorded in the whole wear cycle, as shown in **Figure 3**. From **Figure 3A**, the friction process was divided into two stages: wear in stage and stable wear stage (Ji et al., 2018). It was observed these two stages were most distinct for the pure HA pellet. With 1 wt% nanocarbon in HA, the low COF stage of 1rGO composite lasted for longer laps, compared with pure HA pellet. When the carbon content was further increased to 2 wt%, the COFs of both 2 rGO and 1 rGO + 1 CNT pellets were further decreased and maintained at lower values. Also, it is interesting to see from **Figure 3B** that during the first 200 laps, there was a significant drop of COF when 2 wt% nanocarbons were introduced. This decrease in the friction response can be explained by the lubrication nature of carbonaceous fillers and was enlarged with higher contents of nanocarbons (Llorente et al., 2016).

Mechanical Properties of the Worn Surface

To study the change in mechanical properties of each composition, nanoindentation was carried out before the wear tests and within the wear track after the wear tests. Schematics of h_m and h_f are shown in **Figure 4A**. The plasticity index (W_p/W_t) was computed and shown in **Figure 4B**. It was observed that the fraction of plastic work was decreased after the wear process and the composites reinforced with nanocarbons had lower values than pure HA. Thus, it is evident that the composites reinforced with nanocarbons had improved reisistance to plastic deformation and exhibits enhanced elastic recovery abilities compared to the pure HA pellets (Oke et al., 2020).

From Archard's Law (Archard, 1953), the surface hardness has long been considered as a major factor affecting the wear properties. From **Figure 4C**, the surface hardness of nanocarbon-reinforced composites was higher than that of pure HA before and after the

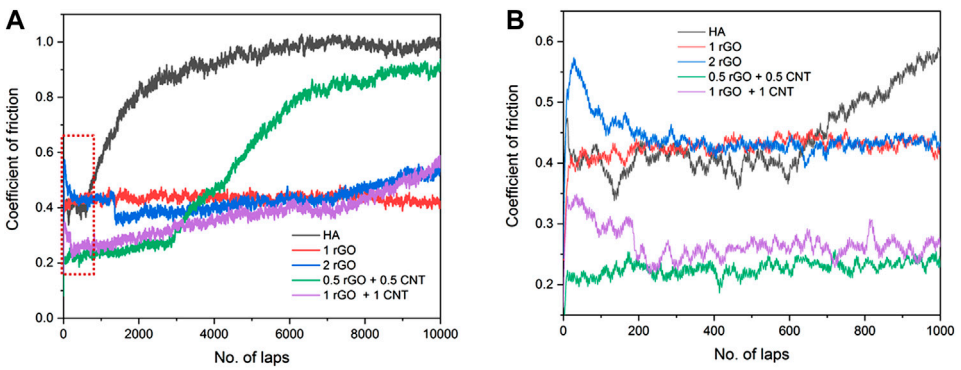

FIGURE 3 | Number of laps vs. coefficient of friction in the tribological tests: **(a)** the whole laps; **(b)** the first 1000 laps. **(b)** is enlarged from dashed rectangle in **(a)**.

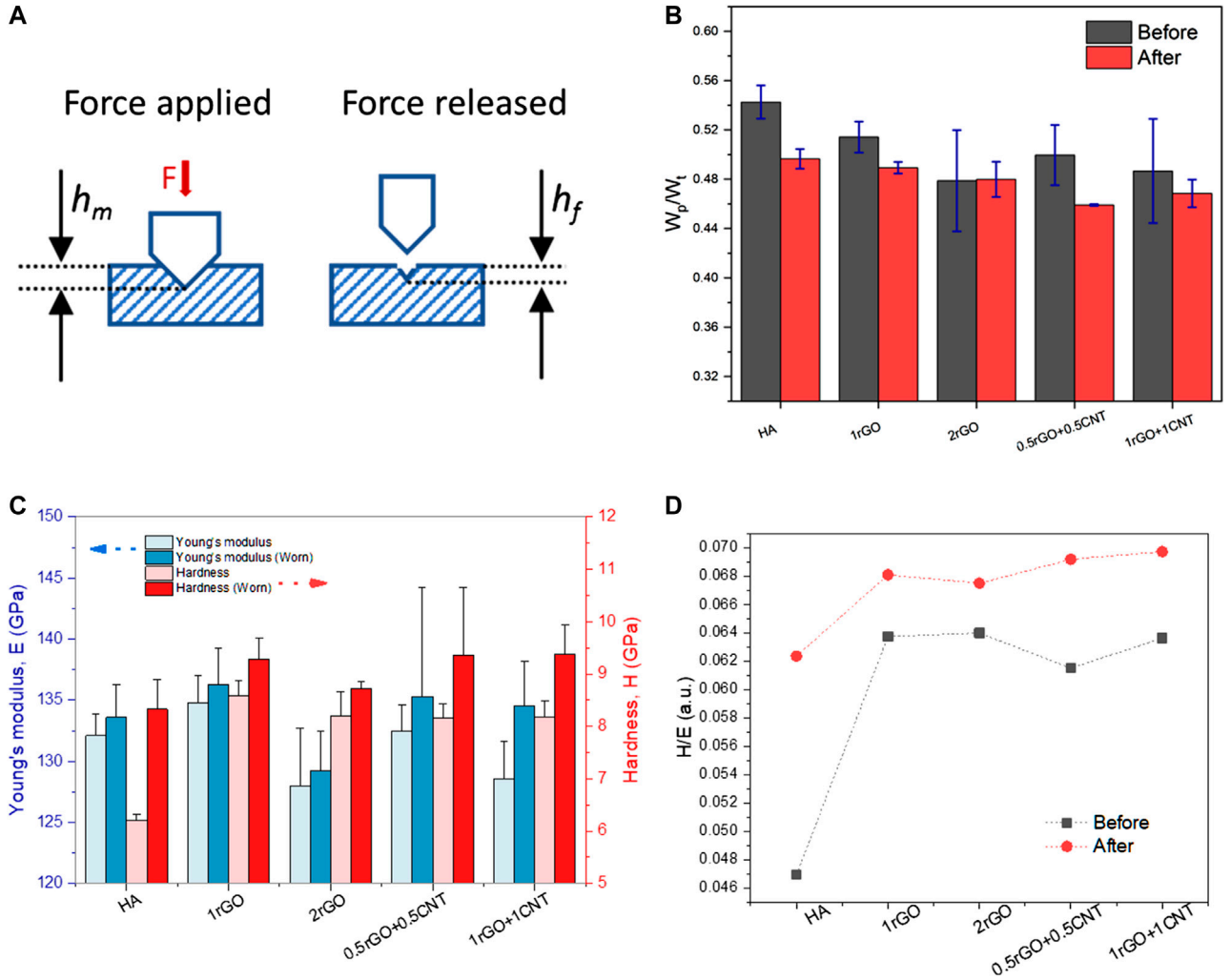

FIGURE 4 | Schematic of the indentation depths at peak load and the final one after elastic recovery **(a)** and the effect of wear process on mechanical properties of sintered samples and worn surfaces in various compositions: **(b)** elastic/plastic behavior, **(c)** elastic modulus and hardness, **(d)** hardness/modulus ratio.

wear tests. The higher worn surface hardness resulted in a considerable reduction in the localized plastic deformation on the worn surfaces and the wear resistance was improved (Konyashin et al., 2015; Yazdani and Isfahani, 2018).

The hardness over modulus or H/E ratio is a popular parameter to predict a material's tribological properties. In **Figure 4D**, the H/E ratios of the bioceramic pellets before and after wear tests are shown. Before wear tests, the samples' H/E ratios were around 0.062 for nanocarbon reinforced composites and around 0.047 for pure HA samples. Furthermore, on the worn surface, all the H/E ratios were increased and the values in nanocarbon reinforced composites were still higher than that of pure HA.

Raman Spectroscopy

The Raman spectra of HA and the composites before and after wear tests are shown in **Figure 5** and the identified Raman bands are tabulated in **Table 2**; the Raman bands for stoichiometric HA and natural bone were also provided for comparison purposes. For all the spectra, the characteristic peaks of HA were identified, with the strongest peaks close to 961 cm^{-1} assigned to the v_1 vibration of PO_4^{3-}, while the peaks around 430, 1,045, and 590 cm^{-1} were attributed to the $v_2PO_4^{3-}$, $v_3PO_4^{3-}$ and $v_4PO_4^{3-}$ HA bands (Tsuda and Arends, 1994; Koutsopoulos, 2002; Antonakos et al., 2007; Cheng et al., 2019). It was noted that the peak positions of $v_2PO_4^{3-}$, $v_3PO_4^{3-}$, and $v_4PO_4^{3-}$ bands were indexed as the strongest peaks in each group. By comparing the bands belonging to HA before and after the wear tests in each sample, there was no significant wave number change. Additionally, no new peak was detected after the wear tests, meaning the matrix material HA was chemically stable and there was no reaction between HA and Si_3N_4 counterbody in the wear tests.

The presence of carbon bands in Raman spectra of rGO- and rGO + CNT-reinforced composites before and after the wear tests proved the survival of nanocarbons after the sintering and wear processes. The calculated intensity ratios of D peak and G peak (I_D/I_G) are shown in **Table 2** to indicate the degree of structural defects of rGO and CNT. In general, the wear tests led to an increased I_D/I_G ratio due to the generation of new structural defects. This

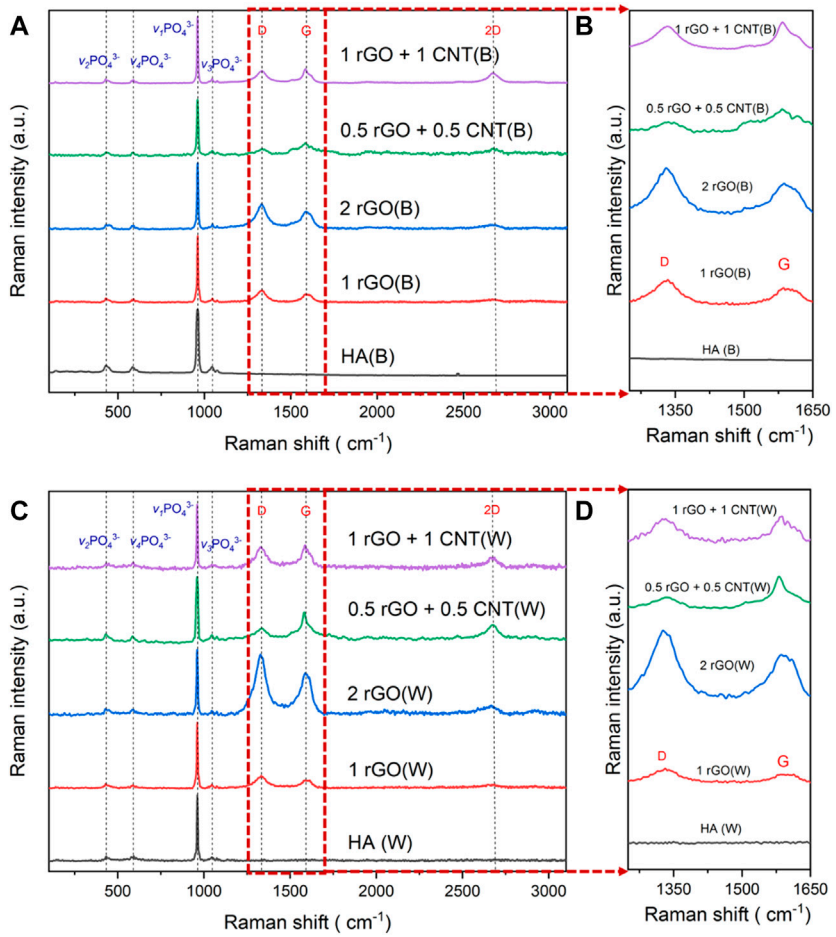

FIGURE 5 | Raman spectra with the main bands and enlarged D and G peaks for: **(a,b)** fresh surfaces before wear test and **(c,d)** worn surfaces.

TABLE 2 | Comparison of Raman band assignments for the intact and worn surfaces of sintered samples, stoichiometric HA, and Bone.

		$v_1PO_4^{3-}$	$v_2PO_4^{3-}$	$v_3PO_4^{3-}$	v_4PO_43-	D	G	2D	I_D/I_G
Intact	HA	962	430	1045	590	-	-	-	-
	HA 1 rGO	961	431	1047	590	1335	1586	2666	1.47
	HA 2 rGO	961	433	1047	588	1329	1588	2670	1.42
	HA 0.5 rGO + 0.5 CNT	960	435	1045	589	1336	1584	2674	0.59
	HA 1 rGO + 1 CNT	960	430	1045	590	1333	1584	2671	1.18
Worn	HA	962	433	1047	592	-	-	-	
	HA 1 rGO	961	430	1046	588	1332	1591	2660	1.78
	HA 2 rGO	961	428	1046	590	1328	1591	2658	1.85
	HA 0.5 rGO + 0.5 CNT	960	431	1046	586	1334	1585	2679	0.58
	HA 1 rGO + 1 CNT	960	433	1046	590	1326	1588	2666	1.43
Reference	Stoichiometric HA (Rincon-Lopez et al. 2018)	964	433	1048	591	-	-	-	-
	Bone (Antonakos, Liarokapis, and Leventouri 2007)	961	432	1044	590	-	-	-	-

increment was directly related to the number of edges and defects, indicating the fragmentation of rGO and/or CNT. By comparing the increment of I_D/I_G ratios caused by the wear process in rGO composites and rGO + CNT composites, the increment was less in the rGO + CNT hybrid- reinforced composites, indicating fewer defects were generated in the rGO + CNT hybrid reinforced composites (Yan et al., 2014; Xiong et al., 2016).

Wear Track Microstructure

The microstructures of wear tracks provide valuable information on the samples' wear properties. The worn surfaces of all samples are shown in **Figure 6**. The surface morphology of the wear tracks clearly indicated that HA and nanocarbon reinforced composites underwent abrasive wear. In pure HA samples, microcracks (1.85 ± 0.61 μm in length) were formed

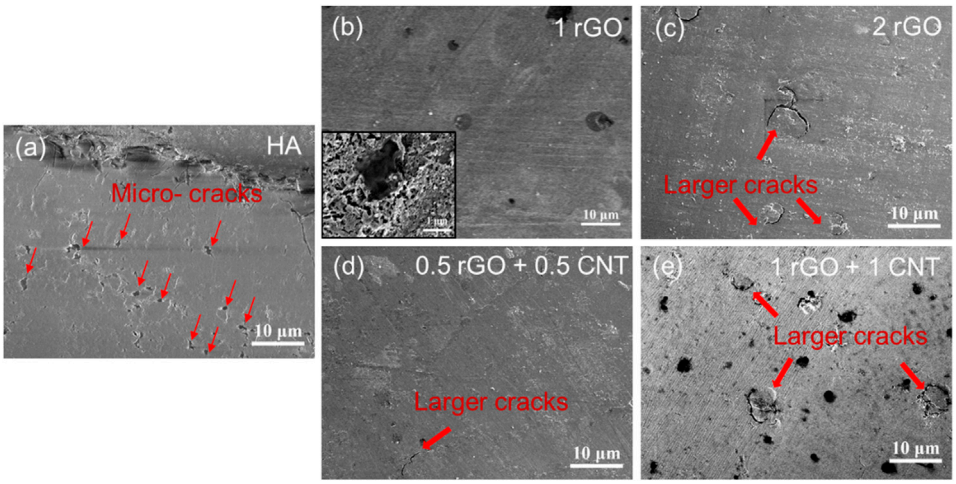

FIGURE 6 | FESEM images of wear tracks: **(a)** HA; **(b)** 1rGO, inset: rGO had strong bonding with HA matrix; **(c)** 2rGO; **(d)** 0.5rGO+0.5CNT; **(e)** 1rGO+1CNT.

randomly in the wear track and it is obvious that the worn surfaces of nanocarbon reinforced composites were smoother than those of the pure HA samples. In nanocarbon-reinforced composites, fewer cracks, albeit in larger sizes (2 rGO: 6.90 ± 2.62 μm in length; 1 rGO + 1 CNT: 5.29 ± 1.02 μm in length), were observed. The reduction in microcracks can be explained by the self-lubricating ability of rGO and CNT that played a vital role in obtaining smoother surface and the larger cracks were possibly formed due to the existence of agglomerating or stacking of nanocarbons (Romanov et al., 2015; Yazdani et al., 2015; Zeinedini et al., 2018).

To study the role played by rGO and CNT in improving the bioceramics' tribological properties, the wear track morphology of HA composites with 2 wt% nanocarbon, in the form of rGO alone or rGO + CNT hybrid, were examined by FESEM under Low Angle Backscatter Electron (LABE) mode (**Figures 7**, **9**). **Figure 7** shows the fresh and worn surfaces of 2 rGO composites. As can be seen in **Figure 7A**, there was a clear boundary between the fresh and worn surfaces, marked with a blue dotted line. The fresh surfaces were flat and dense with no crack, while grooves were parallelly aligned in the worn surface. **Figure 7C** shows the fresh surface at higher magnification,

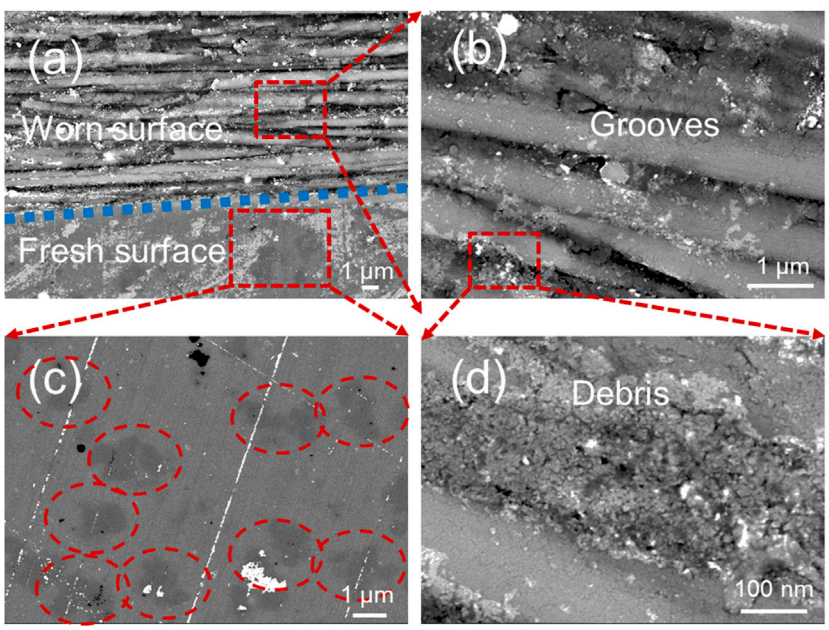

FIGURE 7 | FESEM LABE images of 2rGO composites showing the fresh and worn surfaces: **(a)** fresh and worn surfaces at lower magnification; **(b,d)** worn surfaces at higher magnifications; **(c)** fresh surface at higher magnification.

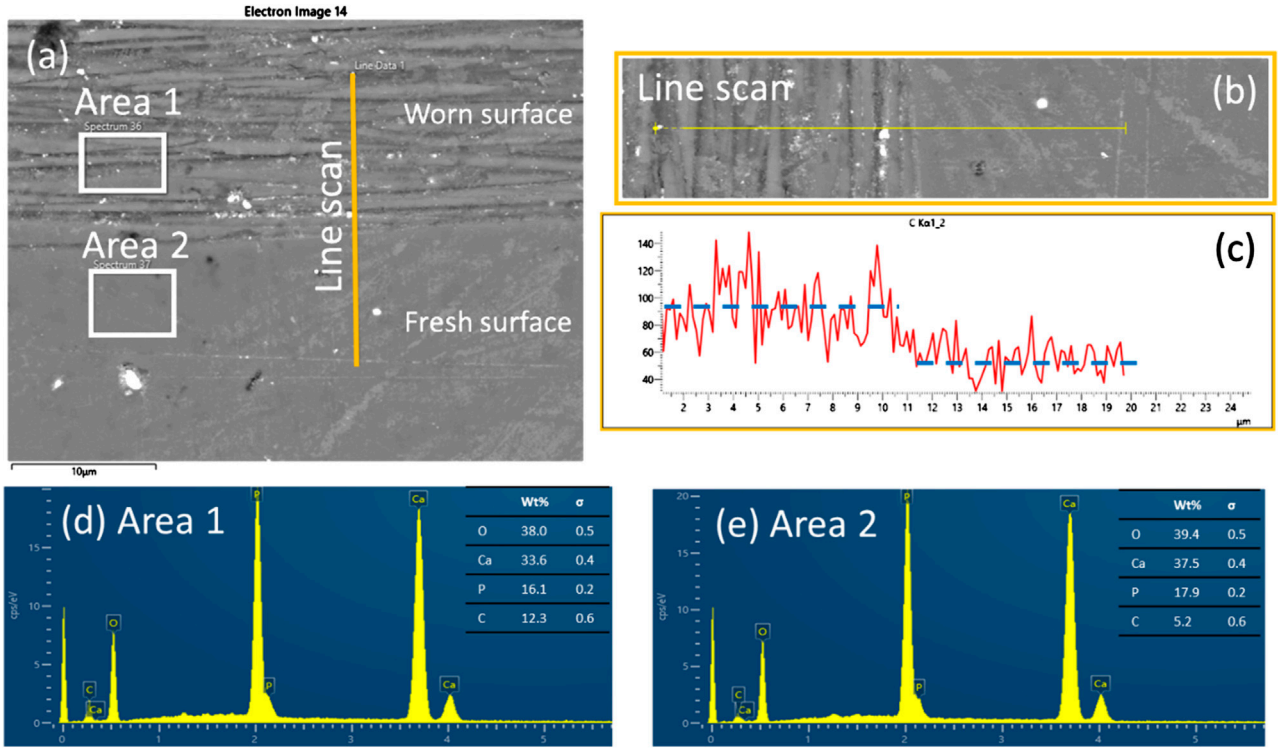

FIGURE 8 | EDS analysis of the fresh and worn surfaces of 2rGO composites: **(a)** electron image; **(b,c)** line element scan; **(d,e)** area element scans.

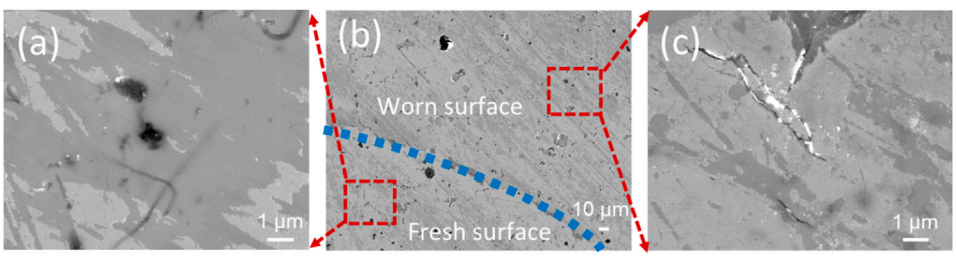

FIGURE 9 | FESEM LABE images of 1rGO+1CNT composites showing the fresh and worn surfaces: **(a)** the fresh surface at high magnification; **(b)** the fresh and worn surfaces at low magnifications; **(c)** the worn surface at high magnification.

where the shaded areas (circled in red) indicated the distribution of rGO in HA. **Figures 7B,D** shows the worn surfaces, and fragments of rGO were found to attach firmly in the grooves. This confirmed the strong bonding between rGO and HA, and proved that rGO could survive the harsh wear process.

The formation of tribofilm was also supported by EDS analysis, as shown in **Figure 8**. Both the EDS line element scan and area element scans confirmed the variation of carbon atom concentration induced by the wear process. The carbon atom concentration showed a significant drop from wear track to the fresh surface in the line scan (**Figures 8B,C**) and the carbon concentration values given by the area element scans taken ~15 μm away from the line scan showed the same trend (**Figures 8D,E**). Although EDS analysis is not quantitative, it can provide reliable information for comparing the relative carbon content in different areas analyzed under the same conditions on the same sample. Furthermore, all the atoms detected in EDS belonged to HA (calcium, phosphate, and oxygen) or rGO/CNT (carbon and oxygen), and no silicon or nitrogen atoms were detected. Thus, it is further confirmed by EDS that there was no reaction between HA and Si_3N_4 counter ball during the wear process. The EDS results indicated the formation of a uniform carbon-rich layer after the wear process in 2 rGO composites. The formation of a tribofilm also explained the reduction of COF as discussed previously (Wu et al., 2019).

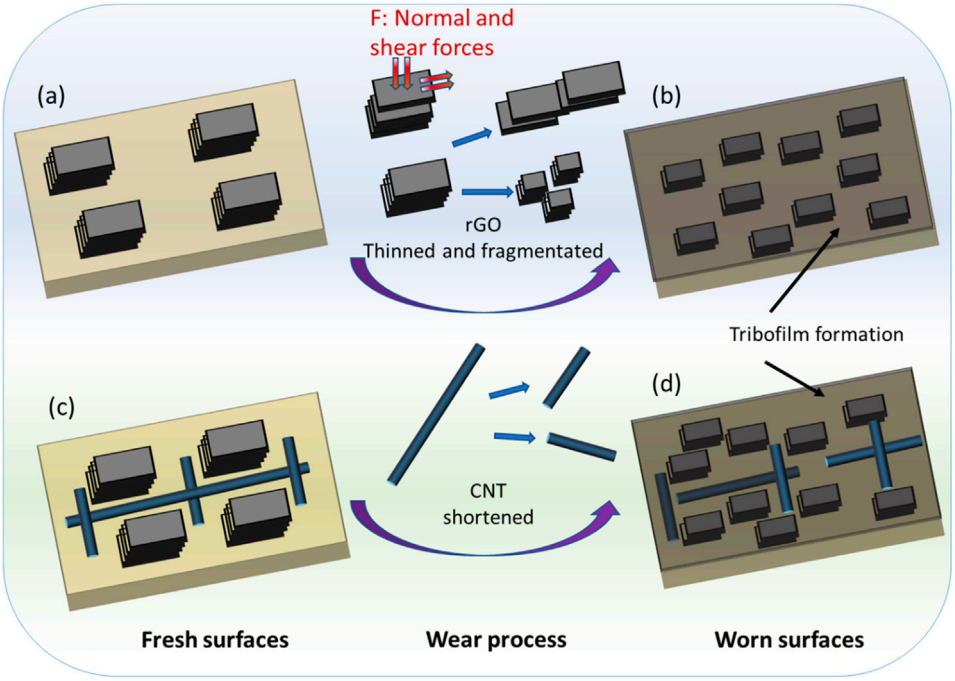

FIGURE 10 | Schematic illustration of the surfaces before and after wear tests: **(a,b)** rGO reinforced HA composites; **(c,d)** rGO + CNT reinforced HA composites.

Figure 9 shows the fresh and worn surfaces of the 1 rGO + 1 CNT composites. As shown in **Figure 9B**, a boundary between fresh and worn surfaces was marked by the dotted blue line. The fresh surface, shown in **Figure 9A**, was as smooth as those of 2 rGO composites. Simultaneously, CNT bridging between HA and rGO that could reduce the degree of rGO stacking for uniform dispersion of the reinforcements had been seen (Priyadershini et al., 2019). Similarly, tribofilms were formed and composed of rGO and CNT.

DISCUSSION

The arrangement of carbon layers in CNT and rGO determined the behaviors of these two nanomaterials during the ball-on-disk tests. Treating the contact configuration between the Si_3N_4 ball and test surface as sphere on plate contact, we calculated the contact pressure. The maximum Hertzian contact pressure (p_{max}) (Greenwood and Tripp, 1967) was 736.9 MPa, and the max shear stress (τ_{max}) was 228.5 MPa within the bioceramic pellets. McAllister et al. (2007) calculated the pressure needed to overcome Van der Waals binding between adjacent layers in GO sheets and graphene sheets, which was 2.5 and 7.2 MPa, respectively. For multiwall CNTs, the removal of a single graphene layer from multiwall CNT requires a force in the range of 11–63 GPa (Yu, 2000). During the wear tests, rGO was fragmented into smaller and thinner pieces, while the peeling of CNT walls was restricted by the concentric arrangement of the layers; therefore, only breaking of CNT occurred. The above calculations indicated that rGOs, which were delaminated during the wear test, served as protecting films, and that CNTs were cut off and fell off the Si_3N_4 counter surface.

According to Yazdani et al. (2015) and Min et al. (2018), CNT and graphene served as micro-bearings that transfer the friction force between counterbody and test surface to rolling and sliding forces to reduce COFs and wear rates when graphene and CNT hybrids were used as reinforcements in composite mateirals. As a result, rGO and CNT were ground on the test surfaces and a solid lubricant film composed of carbon was formed. The formation of tribofilm was in accordance with the COF results that there was a significant drop of COFs in the first 200 laps in the composites with 2 wt% nanocarbon addition. The reduction in wear rate should be attributed to the change of contact between the two sliding surfaces from HA-to-Si_3N_4 contact to carbon protected HA-to-Si_3N_4 contact. From Reye's hypothesis, or energy dissipative hypothesis, with the sliding distance and normal force fixed, the work done was proportional to the integration of the COF during the whole wear cycle. The reduction of COF resulted from the formation of tribofilm reduced the total work done during the test and thus contributed to improved wear behaviors (Flores, 2009).

Moreover, pressure on the tribosurface could be transferred effectively from the matrix to the strong rGOs and CNTs. Usually, the reinforcements act as load-bearing components at contact surfaces which tend to protect the surface from being plowed during sliding (Dorri Moghadam et al., 2015). **Figure 4** suggested that the wear process had a more obvious influence on the surface mechanical properties in nanocarbon reinforced composites than on pure HA, in terms of elasticity, hardness, elastic modulus, and the H/E ratio. In the wear process, if the portion of elastic behavior is increased, the boundary between stick and slip zones moves less, and wear is reduced (Archard, 1957; Hu et al., 2016). Furthermore, materials with higher elastic resilience would absorb more energy

to reduce crack and recover after wear tests (Sherif and Almufadi, 2016; Choi et al., 2017). As a result, the resistance of the bioceramics to plastic deformation was improved with the addition of rGO and CNT, and the wear resistance of the composites was further enhanced. By comparing the wear rate and mechanical properties, it can be concluded that the higher elasticity, hardness, and H/E ratio were favorable to enhance the composites' wear resistance.

The incorporation of rGO and rGO + CNT hybrids as reinforcements in HA bioceramic both reduced the friction between sintered pellets and Si_3N_4 counter ball, and improved the sintered pellets' wear resistance. A tribo film was formed during the wear process due to the thinning and pinning effects of rGO and CNT. In Raman spectra, the G band shifts to higher wavenumber when the number of layers decreases (Wu et al., 2018; McCreary et al., 2019). After the wear tests, the G bands had positive shifting in all the nanocarbon reinforced composites, confirming the thinning of nanocarbons induced by the wear process. As a result, friction was lower due to the lubrication nature of rGO and CNT, and local hardening was introduced with higher hardness and H/E ratio. Both the higher stability and larger lubrication area of the hybrid carbons contributed to the improved friction and wear properties (Yan et al., 2014; Li Y. et al., 2015). In addition, CNT facilitated in achieving uniform distribution of reinforcements in the composites and the pinning effects of CNT enhanced the connection between rGO and HA, making the composites more resistant to wear. A schematic illustration of the above wear process for the composites reinforced with rGO and rGO + CNT hybrids is shown in **Figure 10**.

CONCLUSION

When rGO and rGO + CNT hybrids are introduced as reinforcements in HA bioceramic, the wear and friction performances of the composites were strongly dependent on nanocarbon content and morphology. By increasing the total nanocarbon loadings from 1 wt% to 2 wt%, the wear resistance of both rGO and rGO + CNT reinforced composites was substantially increased. With 2 wt% total nanocarbon content and the nanofiller morphology as rGO/CNT hybrids, the wear rate was reduced by 94.1%. The primary reinforcing mechanism was the formation of carbonaceous films between the composite surfaces and counterbody that served as solid lubrication films. The formation of tribo film was confirmed by FESEM, EDS, and Raman spectra analyses. The tribo film resulted in lower coefficient of friction, higher hardness, and hardness/modulus ratio that contributed to the improved wear performance.

DATA AVAILABILITY STATEMENT

The datasets presented in this study can be found in online repositories. The names of the repository/repositories and accession number(s) can be found below: https://dr.ntu.edu.sg/handle/10356/136922.

AUTHOR CONTRIBUTIONS

HH, ZL, and KAK contributed to the design and implementation of the research. WS helped with the wear tests. RL and HL aided in interpreting the data. HH and ZL wrote the manuscript. KAK obtained the funding. All authors reviewed and proofread the manuscript.

FUNDING

This work was supported by Nanyang Technological University Singapore (Grant No. M4080160) and Ministry of Education, Singapore (AcRF Tier 1 Grant RG141/17).

REFERENCES

Ahmad, I., Anwar, S., Xu, F., and Zhu, Y. (2018). Tribological investigation of multilayer graphene reinforced alumina ceramic nanocomposites. *J. Tribol.* 141, 022002. doi:10.1115/1.4041303

Amini, A. R., Laurencin, C. T., and Nukavarapu, S. P. (2012). Bone tissue engineering: recent advances and challenges. *Crit. Rev. Biomed. Eng.* 40, 363–408. doi:10.1615/critrevbiomedeng.v40.i5.10

Aminzare, M., Eskandari, A., Baroonian, M. H., Berenov, A., Razavi Hesabi, Z., Taheri, M., et al. (2013). Hydroxyapatite nanocomposites: synthesis, sintering and mechanical properties. *Ceram. Int.* 39, 2197–2206. doi:10.1016/j.ceramint.2012.09.023

Antonakos, A., Liarokapis, E., and Leventouri, T. (2007). Micro-Raman and FTIR studies of synthetic and natural apatites. *Biomaterials* 28, 3043–3054. doi:10.1016/j.biomaterials.2007.02.028

Archard, J. (1957). Elastic deformation and the laws of friction. *Proc. Roy. Soc. Lond. Math. Phys. Sci.* 243, 190–205. doi:10.1098/rspa.1957.0214

Archard, J. F. (1953). Contact and rubbing of flat surfaces. *J. Appl. Phys.* 24, 981–988. doi:10.1063/1.1721448

Balani, K., Harimkar, S. P., Keshri, A., Chen, Y., Dahotre, N. B., and Agarwal, A. (2008). Multiscale wear of plasma-sprayed carbon-nanotube-reinforced aluminum oxide nanocomposite coating. *Acta Mater.* 56, 5984–5994. doi:10.1016/j.actamat.2008.08.020

Baradaran, S., Moghaddam, E., Basirun, W. J., Mehrali, M., Sookhakian, M., Hamdi, M., et al. (2014). Mechanical properties and biomedical applications of a nanotube hydroxyapatite-reduced graphene oxide composite. *Carbon* 69, 32–45. doi:10.1016/j.carbon.2013.11.054

Beake, B. D., and Liskiewicz, T. W. (2013). Comparison of nano-f`retting and nano-scratch tests on biomedical materials. *Tribol. Int.* 63, 123–131. doi:10.1016/j.triboint.2012.08.007

Bianco, A. (2013). Graphene: safe or toxic? The two faces of the medal. *Angew. Chem. Int. Ed.* 52, 4986–4997. doi:10.1002/anie.201209099

Cheng, G., Zhang, Y., Yin, H., Ruan, Y., Sun, Y., and Lin, K. (2019). Effects of strontium substitution on the structural distortion of hydroxyapatite by rietveld refinement and Raman spectroscopy. *Ceram. Int.* 45, 11073–11078. doi:10.1016/j.ceramint.2019.02.194

Cheng, Y.-T., and Cheng, C.-M. (2004). Scaling, dimensional analysis, and indentation measurements. *Mater. Sci. Eng. R Rep.* 44, 91–149. doi:10.1016/j.mser.2004.05.001

Choi, G. M., Jin, J., Shin, D., Kim, Y. H., Ko, J. H., Im, H. G., et al. (2017). Flexible hard coating: glass-like wear resistant, yet plastic-like compliant, transparent protective coating for foldable displays. *Adv. Mater.* 29 (19). 1700205 doi:10.1002/adma.201770131

Dorri Moghadam, A., Omrani, E., Menezes, P. L., and Rohatgi, P. K. (2015). Mechanical and tribological properties of self-lubricating metal matrix nanocomposites reinforced by carbon nanotubes (CNTs) and graphene - a review. *Compos. Part B Eng.* 77, 402–420. doi:10.1016/j.compositesb.2015.03.014

Fellah, M., Abdul Samad, M., Labaiz, M., Assala, O., and Iost, A. (2015). Sliding friction and wear performance of the nano-bioceramic α-Al2O3 prepared by high energy milling. *Tribol. Int.* 91, 151–159. doi:10.1016/j.triboint.2015.07.006

Flores, P. (2009). Modeling and simulation of wear in revolute clearance joints in multibody systems. *Mech. Mach. Theor.* 44, 1211–1222. doi:10.1016/j.mechmachtheory.2008.08.003

Gao, C., Feng, P., Peng, S., and Shuai, C. (2017). Carbon nanotube, graphene and boron nitride nanotube reinforced bioactive ceramics for bone repair.*Acta Biomater.* 61, 1–20. doi:10.1016/j.actbio.2017.05.020

Greenwood, J. A., and Tripp, J. H. (1967). The elastic contact of rough spheres. *J. Appl. Mech.* 34, 153–159. doi:10.1115/1.3607616

Gutiérrez-Mora, F., Morales-Rodríguez, A., Gallardo-López, A., and Poyato, R. (2019). Tribological behavior of graphene nanoplatelet reinforced 3YTZP composites. *J. Eur. Ceram. Soc.* 39, 1381–1388. doi:10.1016/j.jeurceramsoc.2018.11.005

Hu, Z., Lu, W., Thouless, M. D., and Barber, J. R. (2016). Effect of plastic deformation on the evolution of wear and local stress fields in fretting. *Int. J. Solid Struct.* 82, 1–8. doi:10.1016/j.ijsolstr.2015.12.031

Huang, Z., Zheng, Z., Zhao, S., Dong, S., Luo, P., and Chen, L. (2017). Copper matrix composites reinforced by aligned carbon nanotubes: mechanical and tribological properties. *Mater. Des.* 133, 570–578. doi:10.1016/j.matdes.2016.08.021

Ji, W., Yuan, Y., Zou, B., Dai, S., and Zhang, H. (2018). Friction and wear behaviour of cemented carbide tool materials sliding against Al 2 O 3 and Si 3 N 4 ceramics under dry condition. *Ceram. Int.* 44, 17486–17491. doi:10.1016/j.ceramint.2018.06.218

Konyashin, I., Ries, B., Hlawatschek, D., Zhuk, Y., Mazilkin, A., Straumal, B., et al. (2015). Wear-resistance and hardness: are they directly related for nanostructured hard materials? *Int. J. Refract. Metals Hard Mater.* 49, 203–211. doi:10.1016/j.ijrmhm.2014.06.017

Koutsopoulos, S. (2002). Synthesis and characterization of hydroxyapatite crystals: a review study on the analytical methods. *J. Biomed. Mater. Res.* 62, 600–612. doi:10.1002/jbm.10280

Lahiri, D., Singh, V., Keshri, A. K., Seal, S., and Agarwal, A. (2010). Carbon nanotube toughened hydroxyapatite by spark plasma sintering: microstructural evolution and multiscale tribological properties. *Carbon* 48, 3103–3120. doi:10.1016/j.carbon.2010.04.047

Li, M., Xiong, P., Yan, F., Li, S., Ren, C., Yin, Z., et al. (2018). An overview of graphene-based hydroxyapatite composites for orthopedic applications. *Bioact. Mater.* 3, 1–18. doi:10.1016/j.bioactmat.2018.01.001

Li, N., Cheng, Y., Song, Q., Jiang, Z., Tang, M., and Cheng, G. (2014). Graphene meets biology. *Chin. Sci. Bull.* 59, 1341–1354. doi:10.1007/s11434-014-0158-0

Li, X., Liang, J., Shi, T., Yang, D., Chen, X., Zhang, C., et al. (2020). Tribological behaviors of vacuum hot-pressed ceramic composites with enhanced cyclic oxidation and corrosion resistance. *Ceram. Int.* 46, 12911–12920. doi:10.1016/j.ceramint.2020.02.057

Li, X., Shi, T., Li, B., Chen, X., Zhang, C., Guo, Z., et al. (2019). Subtractive manufacturing of stable hierarchical micro-nano structures on AA5052 sheet with enhanced water repellence and durable corrosion resistance. *Mater. Des.* 183, 108152. doi:10.1016/j.matdes.2019.108152

Li, Y., Peng, Z., Larios, E., Wang, G., Lin, J., Yan, Z., et al. (2015). Rebar graphene from functionalized boron nitride nanotubes. *ACS Nano.* 9, 532–538. doi:10.1021/nn505792n

Li, Z., Bi, S., Thompson, B. C., Li, R., and Khor, K. A. (2017). Multifunctional bioceramic-based composites reinforced with silica-coated carbon nanotube core-shell structures. *Ceram. Int.* 43, 16084–16093. doi:10.1016/j.ceramint.2017.08.125

Li, Z., Fan, G., Guo, Q., Li, Z., Su, Y., and Zhang, D. (2015). Synergistic strengthening effect of graphene-carbon nanotube hybrid structure in aluminum matrix composites. *Carbon* 95, 419–427. doi:10.1016/j.carbon.2015.08.014

Li, Z., Zhu, W., Bi, S., Li, R., Hu, H., Lin, H., et al. (2020). Incorporating silica-coated graphene in bioceramic nanocomposites to simultaneously enhance mechanical and biological performance. *J. Biomed. Mater. Res.* 108, 1016–1027. doi:10.1002/jbm.a.36880

Liu, Y., Dang, Z., Wang, Y., Huang, J., and Li, H. (2014). Hydroxyapatite/graphene-nanosheet composite coatings deposited by vacuum cold spraying for biomedical applications: inherited nanostructures and enhanced properties. *Carbon* 67, 250–259. doi:10.1016/j.carbon.2013.09.088

Liu, Y., Huang, J., Niinomi, M., and Li, H. (2016). Inhibited grain growth in hydroxyapatite-graphene nanocomposites during high temperature treatment and their enhanced mechanical properties. *Ceram. Int.* 42, 11248–11255. doi:10.1016/j.ceramint.2016.04.038

Llorente, J., Román-Manso, B., Miranzo, P., and Belmonte, M. (2016). Tribological performance under dry sliding conditions of graphene/silicon carbide composites. *J. Eur. Ceram. Soc.* 36, 429–435. doi:10.1016/j.jeurceramsoc.2015.09.040

Lu, Z., Liu, Y., Liu, B., and Liu, M. (2012). Friction and wear behavior of hydroxyapatite based composite ceramics reinforced with fibers. *Mater. Des.* 39, 444–449. doi:10.1016/j.matdes.2012.03.013

Martin, V., and Bettencourt, A. (2018). Bone regeneration: biomaterials as local delivery systems with improved osteoinductive properties. *Mater. Sci. Eng. C* 82, 363–371. doi:10.1016/j.msec.2017.04.038

McAllister, M. J., Li, J.-L., Adamson, D. H., Schniepp, H. C., Abdala, A. A., Liu, J., et al. (2007). Single sheet functionalized graphene by oxidation and thermal expansion of graphite.*Chem. Mater.* 19, 4396–4404. doi:10.1021/cm0630800

McCreary, A., An, Q., Forster, A. M., Liu, K., He, S., Macosko, C. W., et al. (2019). Raman imaging of surface and sub-surface graphene oxide in fiber reinforced polymer nanocomposites. *Carbon* 143, 793–801. doi:10.1016/j.carbon.2018.11.014

Min, C., Liu, D., Shen, C., Zhang, Q., Song, H., Li, S., et al. (2018). Unique synergistic effects of graphene oxide and carbon nanotube hybrids on the tribological properties of polyimide nanocomposites. *Tribol. Int.* 117, 217–224. doi:10.1016/j.triboint.2017.09.006

Notley, S. M., Crawford, R., and Ivanova, E. P. (2013). "Bacterial interaction with graphene particles and surfaces," in *Advances in graphene science*. Editor M. Aliofkhazraei (London, UK: IntechOpen), 100–118.

Oke, S. R., Mphahlele, M. R., Ige, O. O., Falodun, O. E., Okoro, A. M., and Olubambi, P. A. (2020). Structural characterization and nanoindentation studies on mechanical properties of spark plasma sintered duplex stainless steel nanocomposite. *J. Alloys Compd.* 840, 155648. doi:10.1016/j.jallcom.2020.155648

Prakasam, M., Locs, J., Salma-Ancane, K., Loca, D., Largeteau, A., and Berzina-Cimdina, L. (2015). Fabrication, properties and applications of dense hydroxyapatite: a review. *J. Funct. Biomater.* 6, 1099–1140. doi:10.3390/jfb6041099

Priyadershini, S., Rahman, O. S. A., Pandey, K. K., and Keshri, A. K. (2019). Remarkable improvement in tribological behavior of plasma sprayed carbon nanotube and graphene nanoplatelates hybrid reinforced alumina nanocomposite coating. *Ceram. Int.* 45, 5768–5778. doi:10.1016/j.ceramint.2018.12.043

Romanov, V. S., Lomov, S. V., Verpoest, I., and Gorbatikh, L. (2015). Stress magnification due to carbon nanotube agglomeration in composites. *Compos. Struct.* 133, 246–256. doi:10.1016/j.compstruct.2015.07.069

Sherif, H. A., and Almufadi, F. A. (2016). Identification of contact parameters from elastic-plastic impact of hard sphere and elastic half space. *Wear* 368–369, 358–367. doi:10.1016/j.wear.2016.10.006

Teoh, S. H., Thampuran, R., and Seah, W. K. H. (1998). Coefficient of friction under dry and lubricated conditions of a fracture and wear resistant P/M titanium-graphite composite for biomedical applications. *Wear* 214, 237–244. doi:10.1016/s0043-1648(97)00231-7

Thompson, B. C., Murray, E., and Wallace, G. G. (2015). Graphite oxide to graphene. Biomaterials to bionics.*Adv. Mater.* 27, 7563–7582. doi:10.1002/adma.201500411

Tsuda, H., and Arends, J. (1994). Orientational micro-Raman spectroscopy on hydroxyapatite single crystals and human enamel crystallites. *J. Dent. Res.* 73, 1703–1710. doi:10.1177/00220345940730110501

Turan, M. E., Zengin, H., and Sun, Y. (2019). Dry sliding wear behavior of (MWCNT + GNPs) reinforced AZ91 magnesium matrix hybrid composites. *Met. Mater. Int.* 26, 541–550. doi:10.1007/s12540-019-00338-8

Turnbull, G., Clarke, J., Picard, F., Riches, P., Jia, L., Han, F., et al. (2018). 3D bioactive composite scaffolds for bone tissue engineering. *Bioact. Mater.* 3, 278–314. doi:10.1016/j.bioactmat.2017.10.001

Wang, B., Fu, Q., Yin, T., Li, H., Qi, L., and Fu, Y. (2018). Grafting CNTs on carbon fabrics with enhanced mechanical and thermal properties for tribological applications of carbon fabrics/phenolic composites. *Carbon* 139, 45–51. doi:10.1016/j.carbon.2018.06.032

Wang, W., and Yeung, K. W. K. (2017). Bone grafts and biomaterials substitutes for bone defect repair: a review. *Bioact. Mater.* 2, 224–247. doi:10.1016/j.bioactmat.2017.05.007

Wu, J.-B., Lin, M.-L., Cong, X., Liu, H.-N., and Tan, P.-H. (2018). Raman spectroscopy of graphene-based materials and its applications in related devices. *Chem. Soc. Rev.* 47, 1822–1873. doi:10.1039/c6cs00915h

Wu, P., Chen, X., Zhang, C., and Luo, J. (2019). Synergistic tribological behaviors of graphene oxide and nanodiamond as lubricating additives in water. *Tribol. Int.* 132, 177–184. doi:10.1016/j.triboint.2018.12.021

Xiong, C., Li, T., Dang, A., Zhao, T., Li, H., and Lv, H. (2016). Two-step approach of fabrication of three-dimensional MnO2-graphene-carbon nanotube hybrid as a binder-free supercapacitor electrode. *J. Power Sources* 306, 602–610. doi:10.1016/j.jpowsour.2015.12.056

Yan, Z., Peng, Z., Casillas, G., Lin, J., Xiang, C., Zhou, H., et al. (2014). Rebar graphene. *ACS Nano* 8, 5061–5068. doi:10.1021/nn501132n

Yazdani, A., and Isfahani, T. (2018). Hardness, wear resistance and bonding strength of nano structured functionally graded Ni-Al2O3 composite coatings fabricated by ball milling method. *Adv. Powder Technol.* 29, 1306–1316. doi:10.1016/j.apt.2018.02.025

Yazdani, B., Xu, F., Ahmad, I., Hou, X., Xia, Y., and Zhu, Y. (2015). Tribological performance of Graphene/Carbon nanotube hybrid reinforced Al2O3 composites. *Sci. Rep.* 5, 11579. doi:10.1038/srep11579

Yu, M. (2000). Strength and breaking mechanism of multiwalled carbon nanotubes under tensile load. *Science* 287, 637–640. doi:10.1126/science.287.5453.637

Zeinedini, A., Shokrieh, M. M., and Ebrahimi, A. (2018). The effect of agglomeration on the fracture toughness of CNTs-reinforced nanocomposites. *Theor. Appl. Fract. Mech.* 94, 84–94. doi:10.1016/j.tafmec.2018.01.009

Zhao, Q., Gan, X., and Zhou, K. (2019). Enhanced properties of carbon nanotube-graphite hybrid-reinforced Cu matrix composites via optimization of the preparation technology and interface structure. *Powder Technol.* 355, 408–416. doi:10.1016/j.powtec.2019.07.055

Conflict of Interest: The authors declare that the research was conducted in the absence of any commercial or financial relationships that could be construed as a potential conflict of interest.